Elastic properties, thermal stability, and thermodynamic parameters of MoAlB

Sankalp Kota,[1] Matthias Agne,[2] Eugenio Zapata-Solvas,[3] Olivier Dezellus,[4] Diego Lopez,[5] Bruno Gardiola,[4] Miladin Radovic,[5] and Michel W. Barsoum[1,*]

[1]*Department of Materials Science and Engineering, Drexel University, Philadelphia, Pennsylvania 19104, USA*
[2]*Department of Materials Science and Engineering, Northwestern University, Evanston, Illinois 60208, USA*
[3]*Centre for Nuclear Engineering & Department of Materials, Imperial College London, London SW7 2AZ, United Kingdom*
[4]*Laboratoire des Multimatériaux et Interfaces, Université Claude Bernard LYON1, UMR CNRS 5615, F-69622 Villeurbanne, France*
[5]*Department of Mechanical Engineering, Texas A&M University, College Station, Texas 77843, USA*

MoAlB is the first and, so far, the only transition-metal boride that forms alumina when heated in air and is thus potentially useful for high-temperature applications. Herein, the thermal stability in argon and vacuum atmospheres and the thermodynamic parameters of bulk polycrystalline MoAlB were investigated experimentally. At temperatures above 1708 K, in vacuum and inert atmospheres, this compound incongruently melts into the binary MoB and liquid aluminum metal as confirmed by differential thermal analysis, quenching experiments, x-ray diffraction, and scanning electron microscopy. Making use of that information together with heat-capacity measurements in the 4–1000-K temperature range—successfully modeled as the sum of lattice, electronic, and dilation contributions—the standard enthalpy, entropy, and free energy of formation are computed and reported for the full temperature range. The standard enthalpy of formation of MoAlB at 298 K was found to be -132 ± 3.2 kJ/mol. Lastly, the thermal conductivity values are computed and modeled using a variation of the Slack model in the 300–1600-K temperature range.

I. INTRODUCTION

Transition-metal borides (TMBs) are prized refractory materials for their high melting points, high hardness, and excellent electrical and thermal conductivities. These properties, among others, make them useful for applications ranging from wear-resistant coatings [1], refractory crucibles, high-temperature (HT) electrodes [2], solar absorbers [3], permanent magnets [4], and primary battery electrodes [5–7]. Despite renewed interest in the binary TMBs for structural aerospace components related to hypersonic flight and atmospheric reentry of space vehicles, these compounds in their nominally pure form suffer from poor oxidation resistance in air above 1200 °C [8,9].

Recently, we reported on the bulk synthesis of a layered ternary transition-metal boride—MoAlB—that forms a protective and adherent alumina Al_2O_3 scale when heated in air at temperatures up to 1400 °C [10]. In that regard, MoAlB overcomes many limitations of binary TMBs and is quite similar to the layered aluminum- (Al-) containing $M_{n+1}AX_n$ (MAX) phases Ti_2AlC, Ti_3AlC_2, and Cr_2AlC, which form highly protective aluminum oxide scales during high-temperature oxidation in air [11–13]. More recently, Chaix-Pluchery *et al.* reported density-functional-theory- (DFT-) calculated phonon density of states (pDOS) of MoAlB and found excellent matches with the peak positions of the experimentally measured Raman spectra [14].

MoAlB has a layered orthorhombic structure consisting of a molybdenum boride (MoB) sublattice, similar to that of the orthorhombic polymorph of MoB, interleaved by two Al layers [15]. Previous work on this compound focused on the growth of MoAlB single crystals and the partial substitution of the Mo site with Cr and W [16–20]. The MoAlB single crystals were shown to have a relatively low hardness (10–13 GPa) compared to most TMBs [19,20] and high room-temperature electrical conductivity [16,19]. In addition to its excellent oxidation resistance, our recent work on bulk MoAlB has shown that it has high electrical and thermal conductivities, room-temperature compressive strengths that are close to 2 GPa, and a thermal expansion coefficient of -9.6×10^{-6} K^{-1}—that is comparable to many other engineering materials (e.g., alumina, yttria-stabilized zirconia, and Ni superalloys) [13,21]. In combination, these properties bode well for the use of MoAlB in HT applications.

However, before such applications can be contemplated, it is vital to know its melting or thermal decomposition temperature. Phase diagrams of the MoAlB system only exist at 1273 K and indicate MoAlB is in an equilibrium phase at that temperature T [22]. We also noted briefly in our previous work that no melting or reaction peaks were observed when MoAlB samples were studied by differential thermal analysis (DTA) up to 1673 K in an Ar atmosphere [10].

Knowing the constant-pressure heat-capacity c_p of a solid over a wide T range is also indispensable for calculating its thermodynamic parameters, understanding its electronic structure, the T dependence of thermal conductivity, and equilibrium phase relations. At low T's, measuring c_p is a well-established technique to estimate the electronic density of states (eDOS) at the Fermi level $N(E_f)$. For metalliclike conductors, the low-T c_p is given by

$$c_p = \gamma T + \beta T^3, \tag{1}$$

where γ and β are the coefficients of electronic and lattice heat capacities, respectively. Following the free-electron model, γ can be related to $N(E_f)$ by

$$N(E_f) = \frac{3\gamma}{\pi^2 k_B^2}, \tag{2}$$

---

*Corresponding author: barsoumw@drexel.edu

where k_B is the Boltzmann constant. Previously, Eq. (1) was used to successfully calculate γ and β of transition-metal borides [23,24] and the MAX phases [25,26].

The purpose of this paper is to thoroughly characterize the thermal and elastic properties of MoAlB. This is accomplished by determining its thermal stability regime in inert and vacuum atmospheres using DTA, x-ray diffraction (XRD), and quenching experiments to determine the phases present above the decomposition temperature. We also measured c_p over the 4–1000-K temperature range using a relaxation method at low temperatures and differential scanning calorimetry (DSC) at high temperatures. A suitable model was found to capture the temperature dependence of c_p. From these results, we estimate the standard enthalpy of the formation of MoAlB and its free-energy functions as well as reevaluated our previously reported temperature dependence of thermal conductivity [10]. We also use resonant ultrasound spectroscopy (RUS) to measure Young's and shear moduli in the 300–1473-K temperature range.

II. EXPERIMENTAL PROCEDURES

A. Sample preparation

Dense predominantly single-phase MoAlB samples were prepared according to a previous report [10]. Briefly, MoB and Al powders were ball milled in a polyethylene container with zirconia milling balls for 24 h. The mixed powders were precompacted under a load corresponding to 30 MPa and then hot pressed in a boron nitride-coated graphite die under vacuum (<13.3 Pa) at $1200\,^{\circ}$C for 5 h under a load corresponding to a stress of 25 MPa. The samples were ground and polished progressively down to 800 grit SiC paper and cut with a diamond wheel to dimensions needed for further characterization.

B. Characterization

At low temperatures, the c_p of a 16.5-mg rectangular sample $\sim$0.6-mm thick was measured by the relaxation method using a Quantum Design physical properties measurement system over the 4–303 K temperature range at a heating rate of 0.2 K/min. The measurement was conducted under vacuum (10^{-3} Pa). At high T's, three measurements were acquired using a DSC (NETZCH, Germany) in the 300–1000-K temperature range with a heating rate of 20 K/min. The DSC was calibrated with a sapphire standard under the same conditions. Two measurements were conducted in a dynamic N_2 atmosphere under a flow of 20 ml/min; the third was conducted in a flowing Ar atmosphere. The samples were placed in either Pt- or Al_2O_3-lined Pt crucibles. The c_p was converted from J/g/K to J/mol/K using the molar mass of 133.73 g/mol. No correction to c_p was made for the small volume fraction of impurity phases known to be present [6 ± 3-vol % Al_3Mo and <3-vol % Al_2O_3, see Fig. 1(a)]. DTA and thermogravimetric analysis (TGA) (Netzsch STA 449F1, Selb, Upper Franconia, Germany) were performed simultaneously under high-purity Ar flow (99.998%-pure) on samples placed in Al_2O_3 crucibles in the 298–1873 K temperature range, heated at a rate of 10 K/min.

Quenching experiments were conducted under a primary vacuum (0.1–1.0 Pa) or static Ar environment (99.999% -pure, 80 kPa) in an induction heated vertical tube furnace equipped with a bichromatic pyrometer for temperature measurement. The MoAlB sample was placed inside a graphite crucible suspended by SiC fibers and an electromagnetic system. After a dwell time at the heat treatment temperature of 1773 K, the electromagnet was switched off, leading to the fall of the graphite crucible and sample directly into cold oil (273 K) without any exposure to air. The sample was then removed from the oil, cleaned with acetone, and dried before further characterizations.

The elastic constants were measured in the 300–1473 K temperature range using a custom-made high-temperature setup for RUS with a RUSPEC control unit (Magnaflux, Glenview, IL). Disks, 18 mm in diameter, 2.5-mm high, were subjected to continuous Ar flow during the testing to prevent their oxidation. The high-temperature setup uses three 6-in. single-crystal alumina rods glued to piezoelectric transducers: one of them to transmit ultrasonic waves in the 20 to 500 kHz frequency range at a constant amplitude to the sample. The other two are used to monitor the signal from the sample. RUSPEC software (Magnaflux, Glenview, IL) was used to determine the elastic constants at each temperature from the collected resonant spectra using a procedure described in more detail elsewhere [27,28]. Since all samples examined in this paper had polycrystalline structures with random orientations, they were treated as isotropic elastic solids. Thus, two elastic constants, namely, Young's (E) and shear (G) moduli were determined directly from the resonant spectra, whereas the bulk modulus (B) was computed from the triadic relation [29,30]: $B = (EG)(9G - 3E)^{-1}$.

XRD was conducted on a powder diffractometer (Rigaku SmartLab, Tokyo, Japan) using Cu $K\alpha_1$ radiation ($\lambda = 1.540\,598$ nm). Scanning parameters were a 0.04° step size 100-s dwelling time per step. The XRD patterns were obtained on the pristine sample's cross section, the sample surfaces after TGA/DTA, and the bulk of the samples after grinding their surfaces with 400 grit SiC paper. Each XRD pattern is normalized with respect to the most intense peak in that pattern. A scanning electron microscope (SEM) (Zeiss Supra 50VP) and energy dispersive x-ray spectroscope (EDS) (Oxford Instruments) were used to image the samples and analyze the impurities present and their relative elemental compositions.

III. RESULTS AND DISCUSSION

A. Sample characterization

Image analysis of backscattered electron images revealed the presence of $\sim$6 $\pm$ 3-vol % $Al_{3+x}Mo_{1-x}$ or Al_8Mo_3 and <3-vol % Al_2O_3 [see Fig. 1(a)]. XRD results showed the sample to be predominantly single-phase MoAlB as shown on the bottom curve of Fig. 1(b). The density of 6.45 g/cm^3 determined by the Archimedes method suggests that all samples were fully dense.

B. Thermal stability

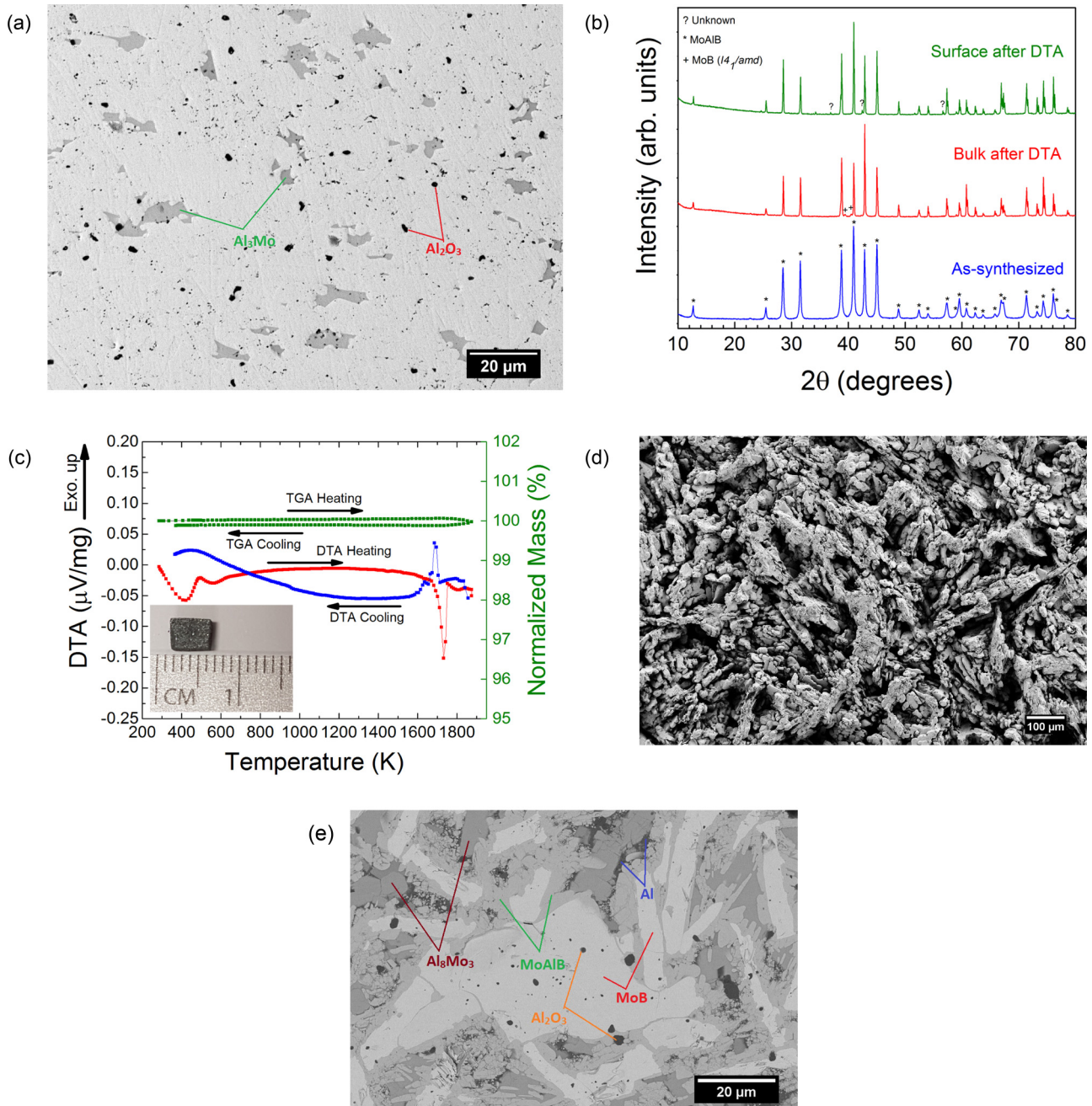A typical DTA/TGA thermogram performed in an Ar atmosphere is shown in Fig. 1(c). At temperatures below

FIG. 1. (a) A backscattered electron micrograph of an as-synthesized and polished MoAlB cross section. (b) XRD on a pristine polished surface (bottom), the sample bulk (middle) after DTA, and surface (top) after DTA. (c) A DTA/TGA thermogram performed under Ar on a dense MoAlB sample. The inset shows a sample after DTA/TGA in Ar. (d) SEM micrograph of bulk cross-sectional morphology after DTA/TGA to 1600 °C under Ar. (e) A micrograph of the sample surface after annealing at and quenching from 1773 K under Ar.

473 K, a small endotherm is present which may be due to the evaporation of adsorbed water from surface pores. Upon further heating above 473 K, relatively little heat flux is observed until a large endothermic peak emerges at 1708 K with a peak temperature of 1743 K. During cooling, a narrower exothermic peak emerges at 1710 K with a peak temperature of 1704 K.

After DTA/TGA in Ar, the cross-sectional area of the sample *increased* by ~50%, and the initially sharp edges of the sample became rounded. In addition, an extremely porous microstructure [Fig. 1(d)] was observed under SEM. EDS

on the cross section after DTA/TGA showed an Al:Mo ratio of (0.85–0.93), which is comparable to that of the pristine sample (0.81–0.85). XRD on the sample bulk [middle curve in Fig. 1(b)] showed narrower peaks and some changes in peak intensity ratios, and the emergence of several low intensity peaks at 39.4° and 40.4° 2θ that correspond to tetragonal MoB (space-group $I4_1/amd$, ICSD No. 24280). XRD of the sample's surface was also consistent with a sample composed of mostly MoAlB with narrowed peaks. A few new peaks— especially those at 36.9° and 42.5° 2θ—could not be assigned to any known phases, despite our best attempt to match them
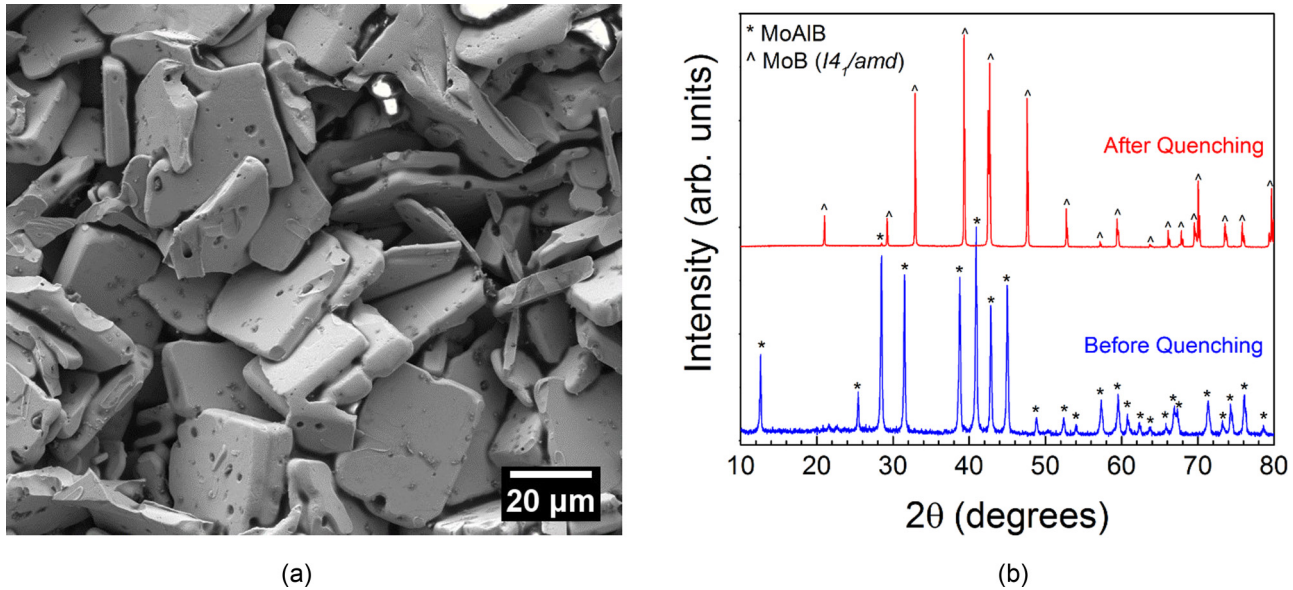
FIG. 2. (a) Micrograph of sample surface after heating at 1773 K for 1 h under vacuum and quenching into cold oil. (b) XRD of the sample surface after annealing under vacuum at 1773 K and quenching.

to phases in the Mo-Al-B-O system. To elucidate the origin of the peaks in DTA, a MoAlB sample was heated at 1773 K for 0.5 h under Ar and quenched into cold oil. A 3.2% weight loss was measured, and the resulting microstructure was still quite dense. The postquench microstructure in this case consisted of MoAlB phase surrounding MoB grains with Al_8Mo_3, Al_2O_3, and Al dispersed uniformly as shown in Fig. 1(e).

The notable peaks in DTA with onsets at 1708 K (exothermic) and 1710 K (endothermic) are similar in area and have a small separation [Fig. 1(c)], and considering the similarity in XRD patterns before and after DTA, the peaks are most likely due to a reversible process. Based on the AlMo phase equilibria reported by Eumann *et al.* [31], neither Al-rich intermetallic impurity phases Al_8Mo_3 nor $Al_{3+x}Mo_{1-x}$ undergo any reactions in or near the 1703–1743-K temperature range. It follows that these peaks are most likely related to a reversible reaction involving MoAlB. The most likely explanation is that MoAlB undergoes a decomposition into MoB and liquid Al during heating and forms again into MoAlB during cooling. The presence of both MoAlB around MoB grains and Al after annealing and quenching under Ar [Fig. 1(e)] also supports the reversibility of the reaction.

Taking into consideration the high wetting angles of liquid Al with most transition-metal borides [32,33], it is likely that the liquid Al formed during decomposition did not wet the MoB surface, causing the observed relatively large expansion of the sample's cross-sectional area. The absence of any major new phases found in the sample bulk after DTA/TGA also supports the proposed decomposition reaction. Interestingly, the postquench microstructure indicates that the cooling rate during quenching was not sufficiently fast to prevent the reformation of MoAlB, giving rise to the core-shell microstructure shown in Fig. 1(e). At this time, the reasons for the differences in microstructures after DTA and after quenching under Ar are unknown and are beyond the scope of this paper.

As a final check of the decomposition reaction, a MoAlB sample was heated to 1773 K and held at that temperature for 1 h under vacuum and then quenched directly into cold vacuum oil. After the experiment, the sample had lost 16% of its initial mass, which accounts for nearly all the initial Al content in MoAlB. Surprisingly, the sample did not crack despite the severity of the thermal shock ($\Delta T = 1500$ K). A representative SEM micrograph of the quenched sample's surface [see Fig. 2(a)] shows a porous microstructure composed of platelike crystals and suggests that large volume changes occurred during this process, in agreement with the DTA experiment. XRD of the quenched sample in Fig. 2(b) shows that almost all the MoAlB had transformed to tetragonal MoB (space-group $I4_1/amd$, ICSD No. 24280). However, no Al-rich phase is detected in this sample, presumably due to its evaporation/sublimation in the vacuum during the dwell time.

Based on the totality of these observations, it is reasonable to conclude that the following incongruent simplified reaction is occurring in this system:

$$\text{MoAlB} \leftrightarrow \text{Al (liquid)} + \text{MoB} \ (T = 1708\,\text{K}). \quad (3)$$

The reaction is simplified in that we assume no solubility of Al in MoB. This is in agreement with the binary phase diagrams that indicate liquid Al and solid MoB are the stable phases at this temperature [31,34]. Interestingly, Sinel'nikova *et al.* note in an early report on MoAlB single-crystal growth that it is an incongruently melting compound [16]. In this scenario, we propose that the phase equilibria relations at 1773 K—after the ternary phase decomposes—is Al-MoB-Mo_3Al_8 (on the Al-rich side) and Al-MoB-MoB_2 (on the B-rich side). At this time, we do not have enough evidence to rule out the direct sublimation of Al especially in vacuum.

C. Heat capacity and thermodynamic properties

Least-squares linear fitting of c_p/T vs T^2 for 72 data points in the 4–11-K range (not shown) yields a γ of 1.94 $\pm$
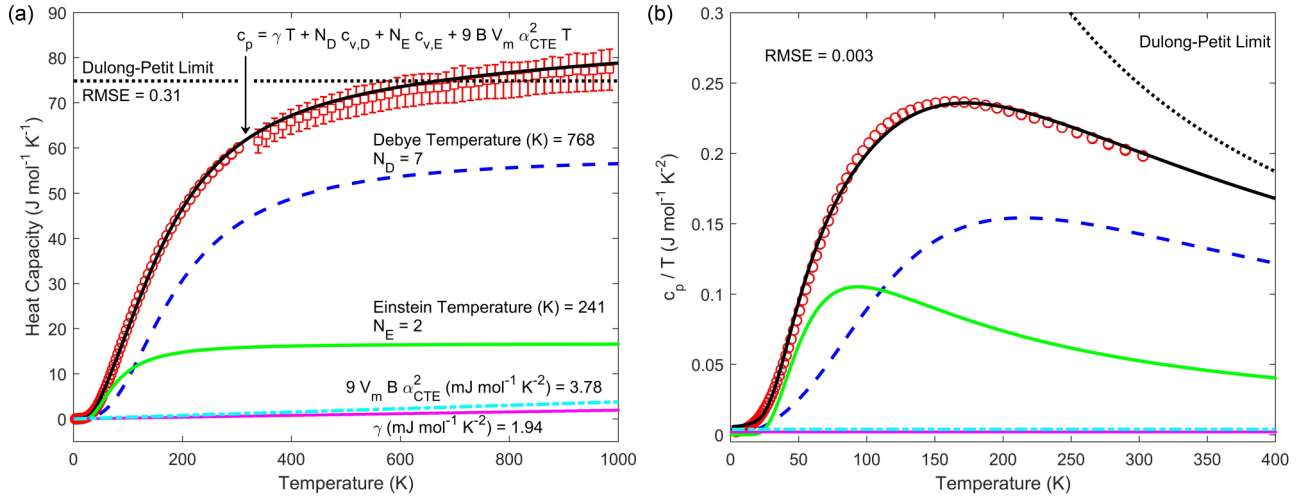
FIG. 3. (a) c_p in the 4–1000-K temperature range (red circles and squares) along with the summation (solid black line) of the constituent Debye-like ($c_{v,D}$, dashed blue curve), Einstein-like ($c_{v,E}$, solid green curve), electronic (γ, purple curve), and dilation ($9V_m\beta\alpha_{CTE}^2$, light blue) contributions. The range of the three high-temperature DSC measurements are shown as error bars. (b) c_p/T vs T for the lower-temperature region demonstrating the quality of the model fit. RMSE stands for root mean square error.

0.01 mJ mol^{-1} K^{-2} and a β of $18.9 \pm 0.5\,\mu$J mol^{-1} K^{-2} according to Eq. (1). From Eq. (2), the eDOS at the Fermi level $N(E_f)$ was calculated to be 3.3 (eV unit cell)$^{-1}$, which is comparable to the value obtained from first principles [3.2 (eV unit cell)$^{-1}$] [35,36] and those of some of the MAX phases [37]. Interestingly, $N(E_f)$ for the binary MoB, which was calculated using the γ reported by Tyan *et al.* [38] (i.e., 2.32 mJ mol^{-1} K^{-2}), is 7.9 (eV unit cell)$^{-1}$ for tetragonal MoB (space-group $I4_1/amd$). From the atomic/orbital projected eDOS calculations (not shown) [35,36], both MoB and MoAlB exhibit B p-band mixing and Mo d-band mixing starting at ≈ 4 eV below E_f. However, the emergence of Al p-band mixing and Mo d-band mixing at ≈ 1.5 eV below E_f in the eDOS of MoAlB is likely responsible for reducing the Mo d contribution to $N(E_f)$.

When c_p is plotted as a function of T, up to 1000 K [Fig. 3(a)], an excellent match is found between the data measured at the low- (open red circles) and the high- (open red squares with error bars) temperature ranges. The uncertainty of the low-temperature measurement is smaller than the size of the markers.

As was performed previously for the MAX phases [39], c_p was modeled as the sum of

$$c_p = \gamma T + N_D c_{v,D} + N_E c_{v,E} + 9B V_m \alpha_{CTE}^2 T, \quad (4)$$

where

$$c_{v,D} = N_D R\,(x_D)^{-3} \int_0^{x_D} [(x^4 e^x)/(e^x - 1)^2]dx$$
$$(x_D \equiv \theta_D/T), \quad (5)$$

and

$$c_{v,E} = N_E R\,(x_E)^2 e^x/(e^x - 1)^2 \quad (x_E \equiv \theta_E/T), \quad (6)$$

where N_D and N_E represent the number of Debye- and Einstein-like modes such that $N_D + N_E = 3N$, where N is the number of atoms in the formula unit ($N = 3$ for MoAlB), and

R is the universal gas constant. B is the average bulk modulus value (220.3 GPa) over the 300–1000-K range (Table I), and α_{CTE} is the experimentally measured coefficient of thermal expansion (9.6×10^{-6} K^{-1} [10]). A least-squares fitting of the experimental c_p data below 305 K, shown as the solid black line in Fig. 3(a), showed that $N_D = 7$ and $N_E = 2$ produced the best fit for c_p when $\theta_D = 768 \pm 1$ and $\theta_E = 241 \pm 0.5$ K, with a root-mean-square error of 0.31 J mol^{-1} K^{-1} per datum. The details of the various contributions to the total also are shown in Fig. 3(a) The green line represents the Einstein model [Eq. (6)], the dashed blue line represents the Debye model [Eq. (5) and the purple and light blue, respectively, represent linear electronic and dilation terms. The quality of the low-T fit is highlighted in the plot of c_p/T vs T [Fig. 3(b)]. Note that, due to the uncertainty in the high-T ($T > 305$-K) c_p values, they were not included in the least-squares regression. Rather, the linear contributions to c_p were fixed by γ, B, and α_{CTE}. When the various contributions are added, they indeed

TABLE I. Temperature dependence of the shear (G), Young's (E), and bulk (B) moduli measured by high-temperatures RUS.

| T (K)	G (GPa)	E (GPa)	B (GPa)	T (K)	G (GPa)	E (GPa)	B (GPa)
300	151.2	372.9	232.9	**923**	141.6	348.2	214.7
323	151.6	372.4	228.3	**973**	140.6	345.8	213.2
373	152.4	372.0	221.9	**1023**	139.5	343.9	214.2
423	151.7	371.1	223.2	**1073**	138.7	342.2	214.1
473	150.9	368.7	220.6	**1123**	137.9	339.6	210.8
523	150.1	367.5	221.8	**1173**	137.1	340.3	219.3
573	148.9	364.6	220.3	**1223**	136.3	338.9	220.1
623	147.8	362.5	221.0	**1273**	133.8	330.5	207.5
673	146.5	360.0	221.2	**1323**	133.8	329.7	205.0
723	145.5	357.7	220.0	**1373**	133.1	327.7	203.1
773	144.5	355.4	218.9	**1423**	131.7	323.3	197.5
823	143.7	353.1	216.6	**1473**	129.8	319.9	198.9
873	142.5	350.6	216.5				
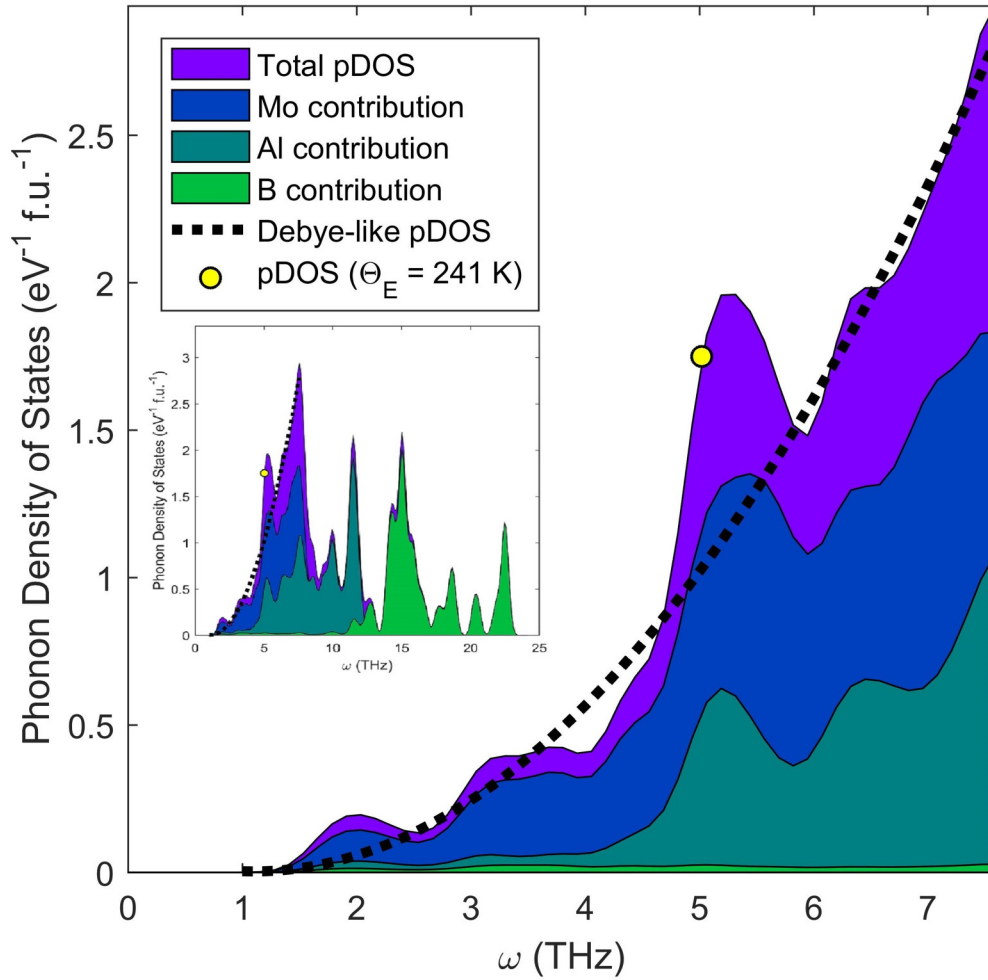
FIG. 4. Total phonon density of states (purple) and the constituent contributions from Mo (blue), Al (teal), and B (green), reported by Chaix-Pluchery *et al.* [14], of the acoustic region as compared to the Debye form of the pDOS (dashed black line). The value of the pDOS evaluated at $\theta_E = 241$ K (5.02 THz) is shown as a yellow circle, which is near the local maximum. Inset shows the phonon density of states over the entire range of frequencies (0–25 THz).

reproduce the experimental data nicely with c_p values quite near the mean of the three DSC measurements, the range of which are shown as error bars in Fig. 3(a).

Note that the necessity to include Einstein-like modes was determined by plotting c_p/T^3 vs T, which was found to have a peak around 48 K (not shown). For a purely Debye-like crystal, $c_{v,D}/T^3$ cannot have a low-temperature peak. $c_{v,E}/T^3$, however, does have a maximum when $\frac{\partial}{\partial T}(\frac{c_{v,E}}{T^3}) = 0$. This can be shown to occur at $T \approx \theta_E/5$, assuming $e^x \gg 1$ in the denominator of Eq. (6). This is precisely the θ_E we find from the least-squares fitting procedure. The number of Einstein-like modes ($N_E = 2$) also was determined by least-squares fitting of Eq. (4) as N_E was increased in integer amounts from 0 to 5. It is important at this juncture to make the distinction that N_D and N_E do *not* represent the actual number of acoustic or optical modes in the phonon dispersion. As there can only be three acoustic modes, $N_D = 7$ does not make physical sense. Furthermore, the 18 phonon modes of MoAlB have recently been characterized by Raman spectroscopy and DFT [14]. Herein, the number of each mode can be thought of as the fractional contribution of that mode type to c_v. That is 7/9 of c_v is contributed by the acoustic branch and 2/9

of c_v is contributed from low-energy optical modes. Lastly, as $\theta_E = 241$ K translates to a frequency of $\omega_E = 5.02$ THz (167.4 cm^{-1}), it compares well with the two lowest zone-center phonon frequencies (170−210 cm^{-1}) found in the Raman spectra and the low-frequency peak in the pDOS calculated from DFT (Fig. 4) [14]. As this peak is found to break the parabolic dispersion (dashed black curve in Fig. 4) that is expected if only acoustic (Debye-like) modes are present, it corroborates our finding that optical (Einstein-like) modes must be included to accurately model the low-T c_p results.

The low-T Debye temperature was calculated from

$$\theta_{D,0} = \left(\frac{12\pi^4 R N_D}{15\beta} \right)^{1/3}. \qquad (7)$$

If N_D is assumed to be 7, $\theta_{D,0} = 621.4$ K; if N_D is assumed to be 9, then $\theta_{D,0} = 675.7$ K. This calculation has the distinct advantage of directly probing the long-wavelength limit of the acoustical phonon dispersion as T approaches 0 K. This has some ramifications for determining the speed of sound in MoAlB as discussed below.
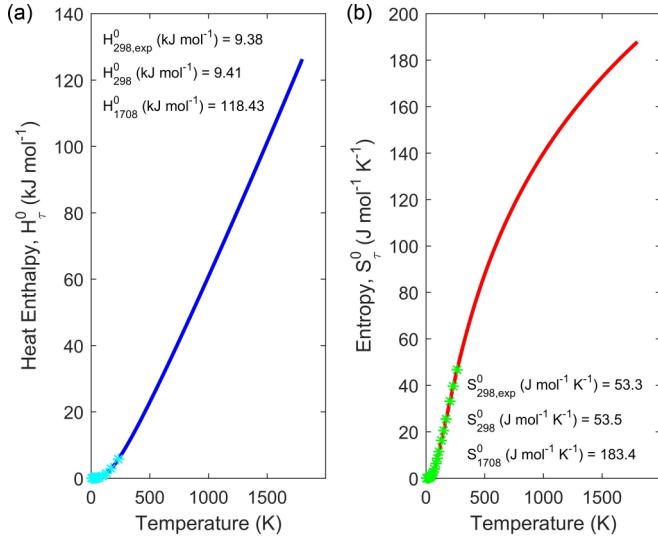
FIG. 5. (a) H^0_{298} calculated from Eq. (8) using experimental low-T c_p data (pale blue markers) and the full-range c_p model (solid blue line) and (b) S^0_{298} calculated according to Eq. (9) using experimental low-T c_p data (green markers) and full-range c_p model (solid red line).

From c_p, the heat enthalpy H^0_τ and entropy S^0_τ can be calculated according to the standard thermodynamics integrations,

$$H^0_\tau = \int_0^\tau c_p(T)dT, \tag{8}$$

$$S^0_\tau = \int_0^\tau \frac{c_p(T)}{T}dT. \tag{9}$$

The standard enthalpy at 298 K H^0_{298} was determined to be 9.38 and 9.41 kJ mol^{-1} from the integration of the experimental c_p and model c_p values, respectively [Fig. 5(a)]. The standard entropy at 298 K S^0_{298} was determined to be 53.3 and 53.5 J mol^{-1} K^{-1} from the integration of the experimental c_p and model c_p values, respectively [Fig. 5(b)]. As the percent difference in both integration results at 298 K was $\approx 0.3\%$ and there was a large measurement uncertainty in the high-temperature c_p data, the model c_p [solid black line in Fig. 3(a)] was used for all further calculations over the entire temperature range.

Combining the results of the DTA, high-temperature quenching experiments, and the model c_p results, the standard enthalpy of formation of MoAlB $\Delta H^0_{f,298}$ was estimated using 1708 K as the reaction temperature for Eq. (3). In an analogous fashion to our previous work on the MAX phase V$_2$AlC [40], $\Delta H^0_{f,298}$ was calculated to be -132.0 ± 3.2 kJ mol^{-1} assuming

$$\Delta H^0_{f,298,\text{MoAlB}} = \Delta G^0_{1708,\text{Al}} + \Delta G^0_{1708,\text{MoB}} - \left(H^0_{1708,\text{MoAlB}} \right.$$
$$\left. - H^0_{298,\text{MoAlB}} \right) + 1708 S^0_{1708,\text{MoAlB}}, \tag{10}$$

where the standard Gibbs free-energy function for phase n at temperature τ has the typical form

$$\Delta G^0_{\tau,n} = \Delta H^0_{\tau,n} - T \Delta S^0_{\tau,n}$$
$$= \Delta H^0_{f,298,n} + \left(H^0_{\tau,n} - H^0_{298,n} \right) - \tau S^0_{\tau,n}. \tag{11}$$

The heat enthalpy $(H^0_\tau - H^0_{298})$ and entropy values for MoB were taken from the continuous functions provided by Bolgar *et al.* [41], and $\Delta H^0_{f,298,\text{MoB}} = -103.9$ kJ mol^{-1} is the value reported by Lavut *et al.* [42]. The thermodynamic values for Al were interpolated from the Joint-Army-Navy-Air Force (JANAF) tables [43]. The uncertainty associated with Eq. (10) (± 3.2 kJ mol^{-1}) was estimated by adding the normalized components of the following considerations:

(i) The uncertainty reported in Ref. [42] for $\Delta H^0_{f,298,\text{MoB}}$ is ± 1.2 kJ mol^{-1}.

(ii) The error in the c_p model due to the uncertainty in γ and the choice of B, resulting in an uncertainty in θ_D and θ_E. The maximum difference in $\Delta H^0_{f,298,\text{MoB}}$, resulting from the linear terms in Eq. (4), was 0.3 kJ mol^{-1}.

(iii) The variance in the c_p model due to the least-squares fitting of the low-T experimental data, resulting in an uncertainty in Eqs. (8) and (9) of $\approx 0.5\%$.

(iv) A nominal uncertainty of 1.0% was assumed for the values taken from Bolgar *et al.* [41] and the JANAF tables [43].

(v) Assuming the reaction temperature is accurate within ± 5 K, its contribution to the uncertainty in Eq. (10) is $<0.2\%$.

From DFT calculations on the Materials Project, the energy of formation at 0 K is -128.8 kJ mol^{-1} [35]. This agrees quite well with the value of -132.0 ± 3.2 kJ mol^{-1} reported herein.

The thermodynamic properties of the MAX phases have been shown to be reasonably approximated from their corresponding MX binary compounds [11]. This follows from the assumption that the M-A bonds are as strong as the M-X bonds. Applying this same approximation to MoAlB,

$$\Delta H^0_{f,298,\text{MoAlB}} \approx \tfrac{3}{2} \Delta H^0_{f,298,\text{MoB}}, \tag{12}$$

we find $\Delta H^0_{f,298,\text{MoAlB}} \approx -155.9$ kJ/mol using the $\Delta H^0_{f,298,\text{MoB}}$ value reported by Lavut *et al.* [42] This estimation suggests that MoAlB is a more stable compound than what our calculation or the DFT values would suggest. This may easily be disproven by relaxing the assumption that the Mo-B bonds are as strong as the Mo-Al ones. Indeed, if we extend our approximation in Eq. (12) to be averaged with the enthalpy of the formation of a MoAl binary,

$$\Delta H^0_{f,298,\text{MoAlB}} \approx \frac{1}{2}\left(\frac{3}{2}\Delta H^0_{f,298,\text{MoB}} + \frac{3}{a+b}\Delta H^0_{f,298,\text{Mo}_a\text{Al}_b} \right), \tag{13}$$

then $\Delta H^0_{f,298,\text{MoAlB}} \approx -124.9$ kJ/mol using the binary MoAl ($\Delta H^0_{f,298,\text{MoAl}} = -62.6$ kJ/mol) [44] or $\Delta H^0_{f,298,\text{MoAlB}} \approx -136.9$ kJ/mol using the binary Mo$_3$Al$_8$ ($\Delta H^0_{f,298,\text{Mo}_3\text{Al}_8} = -432.2$ kJ/mol) [44]. Both values are again in excellent agreement with our calculation. This simple analysis provides further support that the Al atoms are weakly bonded. It is the "rattling" of these atoms that is primarily responsible for the low-energy optical modes that contribute to c_p (Fig. 3).

Having obtained a reliable value for $\Delta H^0_{f,298}$ allows for the calculation of the standard Gibbs free-energy function $\Delta G^0_{\text{MoAlB}}$ [Eq. (11)] and the free energy of the formation of $\Delta G^0_{f,\text{MoAlB}}$, from its elements defined as

$$\Delta G^0_{f,\text{MoAlB}} = \Delta G^0_{\text{MoAlB}} - \Delta G^0_{\text{Mo}} - \Delta G^0_{\text{Al}} - \Delta G^0_{\text{B}}, \tag{14}$$
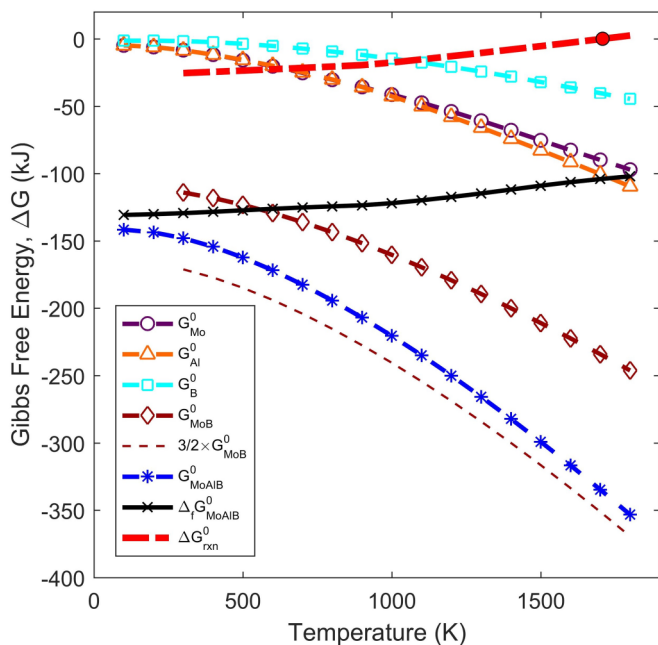
FIG. 6. Standard free-energy function of MoAlB [Eq. (11)], its free energy of formation [Eq. (14)], the free energy of the reaction for Eq. (3), and the constituent standard free energies used in the aforementioned calculations. Also shown is the $(3/2)\Delta G_{MoB}$ approximation (dashed lowest line) resulting in slightly overestimated values as described in the text.

where the free energies of the elements were calculated from the JANAF tables [43]. The results of Eqs. (11) and (14) are plotted for MoAlB in Fig. 6 as dashed dark blue and solid black lines, respectively. For comparison, the same approximation made in Eq. (12) was applied to ΔG_{MoB}^0 in Fig. 6. Not surprisingly, this approximation overestimates the stability of MoAlB.

As a final check on our values, we note that the free energy of the reaction for Eq. (3) ΔG_{rxn}^0, which is just a restatement of Eq. (10), explicitly is as follows:

$$\Delta G_{rxn}^0 = \sum_{products} \Delta G_f^0 - \sum_{reactants} \Delta G_f^0$$

$$= \Delta G_{MoAlB}^0 - \Delta G_{MoB}^0 - \Delta G_{Al}^0 \quad (15)$$

should be equal to zero at 1708 K. Equation (15) is plotted vs temperature in Fig. 5 (dashed red line) and does indeed cross zero at 1708 K (red point in Fig. 5) when MoAlB is no longer the stable phase.

Lastly, to apply these thermodynamic functions to assess the excellent oxidation properties of MoAlB, the free energies of various oxidation reactions were calculated in a manner analogous to Eq. (15) (Fig. 7). Although the pitfall of ZrB$_2$, a promising structural ultra-high-temperature material [8], is the undesirable formation of B$_2$O$_3$ (dashed green line in Fig. 7), which becomes volatile above ≈ 700 K when it melts (green circle in Fig. 7), herein we find that the oxidation reaction for MoAlB proposed by Kota *et al.* [10] (4/3 MoAlB + O$_2$ = 4/3 MoB + 2/3 Al$_2$O$_3$) is the most thermodynamically stable (circle markers in Fig. 7) and that the formation of other/multiple oxides is unlikely (diamond markers in Fig. 7).
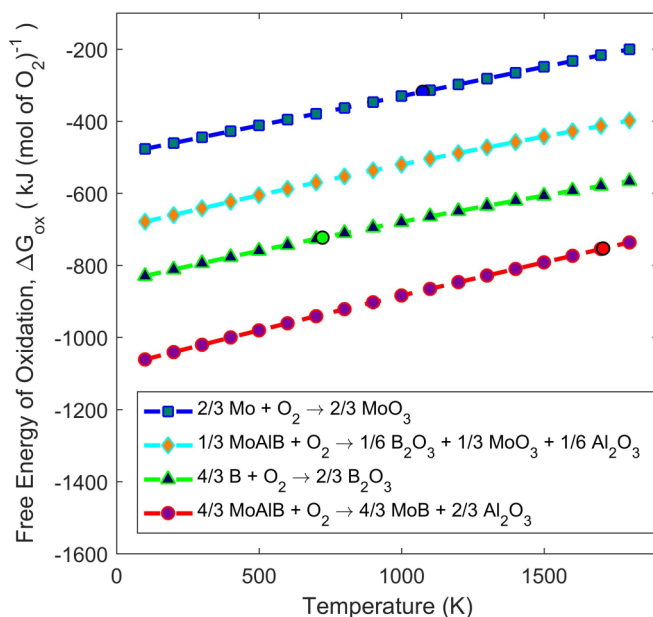

FIG. 7. Free energies of various oxidation reactions listed demonstrating the high stability of the alumina-forming MoAlB compared to the formation of other oxides.

Kinetically, the formation of the Al$_2$O$_3$ layer is proposed to be highly favorable given the weaker Al bonding [implied by Eq. (13)] and the low-frequency vibrations (deduced from θ_E) needed for diffusion. These combined attributes render MoAlB oxidation resistant and hence potentially useful for some high-temperature applications.

D. Thermal transport

In our previous work, we reported the thermal conductivity κ_{tot} as a function of temperature, assuming a c_p based on the Neumann-Kopp rule. Now, using the model c_p values over the full temperature range, we recalculate and replot κ_{tot} (Fig. 8), assuming

$$\kappa_{tot} = D\rho c_p(T), \quad (16)$$

where D is the experimentally measured thermal diffusivity value and ρ is the sample density (6.45 g/cm^3). Based on these results, κ_{tot} is 25.6 W m^{-1} K^{-1} at 373 K and decreases gradually to 22.3 W m^{-1} K^{-1} at 1073 K. In other words, its temperature dependence is relatively weak.

To better understand κ_{tot}, we first calculate the electronic κ_{el} contribution assuming—such as in the MAX phases [45,46], that the Weidman-Franz law viz.,

$$\kappa_{el} = \frac{L_o T}{r(T)} \quad (17)$$

is applicable. In this relationship, L_o is the Lorenz number for a metal, 2.45×10^{-8} W Ω K^{-2}, and $r(T)$ is the temperature-dependent resistivity from Ref. [10], assumed to be linear above 300 K. Once κ_{el} is calculated, the lattice or phonon contribution κ_{latt} to the total is calculated assuming
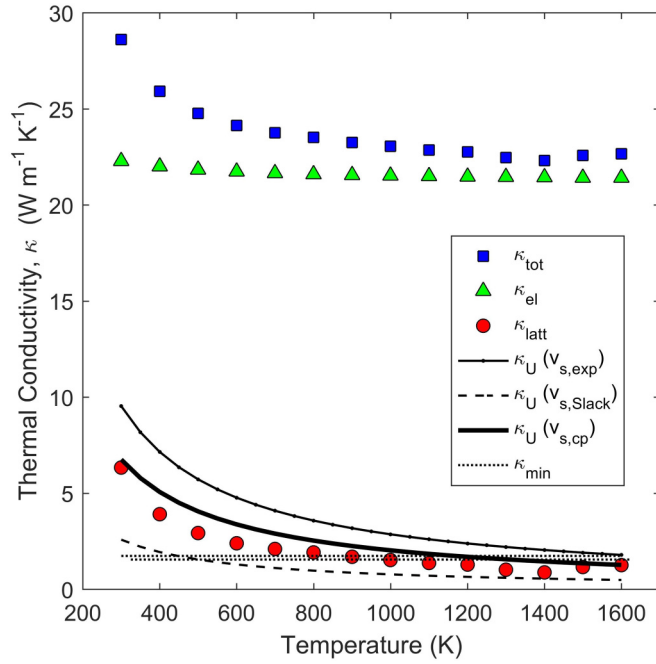
$$\kappa_{latt} = \kappa_{tot} - \kappa_{el}. \quad (18)$$

FIG. 8. Experimentally measured temperature dependence of κ_{tot} (solid blue squares), showing κ_{el} (solid green triangles) and κ_{latt} (solid red circles). Also shown is the κ_{latt} contribution based on the Slack [47] model for thermal conductivity using the speed of sounds v_s estimated from the speed of sound measurements $v_{s,exp}$, the low-temperature Debye temperature $v_{s,cp}$, and from the Slack [47] method $v_{s,Slack}$. The Cahill and Pohl [51] amorphous limit κ_{min} (dotted black line) shows this solid approaches its fundamental limit at high temperatures.

When the various contributions are plotted (Fig. 8), one finds that, at 373 K, κ_{el} accounts for 86% of κ_{tot}. By 1072 K that fraction increases to 96%. Interestingly, in the MAX phases with heavier transition-metal atoms (e.g., Ta_2AlC, Nb_4AlC_3, Nb_2AlC, and Nb_2SnC), the thermal conductivities from phonons are also quite low due to phonon scattering of low-lying modes or rattlers [37].

Here we model κ_{latt} using a variation of the Slack model [47] laid out by Toberer *et al.* [48] for complex materials with no fitting parameters. Assuming the optical mode contributions to κ_{tot} are negligible, the umklapp-limited lattice transport κ_u is given by

$$\kappa_u = \frac{(6\pi)^{2/3}}{4\pi^2} \frac{M v_s^3}{T V^{2/3} \Gamma^2} \frac{1}{n_D}, \tag{19}$$

where v_s is the average speed of sound in the solid, n_D is the number of atoms per unit cell that contribute to the number of Debye-like modes carrying heat ($N_D = 7$), M is the average atomic mass per formula unit, V is the volume per atom, and Γ is the thermodynamic Grüneisen parameter. The latter was estimated assuming

$$\Gamma = \frac{3\alpha_{CTE} B}{c_v \rho}. \tag{20}$$

Approximating c_v by the Dulong-Petit limit viz., $74.82\,J\,mol^{-1}\,K^{-1}$ and using the same average bulk modulus (220.3 GPa) in Eq. (20) yields a Γ of 1.76, which again is comparable to values reported for the MAX phases [37]. The

estimation of v_s, however, is not as straightforward. It is well known that different methods to approximate v_s can result in substantial differences [48,49]. Consequently, we estimate v_s in three different ways:

(i) from the temperature-averaged longitudinal $\bar{v}_l$ and transverse $\bar{v}_t$, speed of the sound measurements used to determine the elastic constants, combined in the manner summarized by Anderson [50],

$$\bar{v}_s = \left[1/3 \left(2/\bar{v}_t^3 + 1/\bar{v}_l^3 \right) \right]^{-1/3}, \tag{21}$$

(ii) from the low-temperature Debye temperature (621 K) determined from β in Eq. (1), which probes the long-wavelength limit of the acoustic phonon dispersion,

(iii) from the Debye temperature as suggested by Hill [30] and Slack [47], calculated from the pDOS $g(\omega)$ shown in Fig. 3,

$$\theta_{\infty,Slack} = \left[\frac{5h^2}{3k_B^2} \frac{\int_0^{\omega_{ac}} \omega^2 g(\omega) d\omega}{\int_0^{\omega_{ac}} g(\omega) d\omega} \right]^{1/2}, \tag{22}$$

where the latter two temperatures can be converted into v_s through the Debye relation,

$$k_B \theta_D = \hbar \omega_D = \hbar \left[6\pi^2 / V_{at} \right]^{1/3} v_s, \tag{23}$$

when ω_D is found in terms of the volume per atom V_{at} by integration of the Debye pDOS [$3/V_{at} = \int_0^{\omega_D} (\frac{3\omega^2}{2\pi^2 v_s^3}) d\omega$]. Carrying out methods (i)–(iii) (above) resulted in v_s values of 5280, 4710, and 2820 m/s, respectively.

Additionally, the minimum lattice thermal conductivity κ_{min} can be estimated according to the Cahill and Pohl approximation for amorphous materials,

$$\kappa_{min} = \left(\frac{3}{2} \right) \left(\frac{\pi}{6 V^2} \right)^{1/3} k_B v_s, \tag{24}$$

which is T independent and only depends on the atomic volume and v_s in the solid [51].

When κ_u and κ_{min} are compared to κ_{latt} (bottom of Fig. 8), the overall agreement is surprisingly good given the simplicity of the model and the approximations that were made. It should be noted that it is generally difficult to extract κ_{latt} for metalliclike materials and that the Slack model [47] was developed for nonmetallic solids. Nevertheless, the $1/T$ dependence of κ_{latt} is a signature of umklapp-dominated processes, the slope of which is matched well between the model and the experiment. Of the three estimations of v_s, we find that the low-temperature Debye temperature [method (ii) above] fits the data the best ($v_s = 4710$ m/s). The Slack [47] estimation of v_s is found to be substantially lower than the other two values, and the resulting κ_u does not share the same slope as our data. As the estimation of Γ is also a likely source of error, further investigations are needed to confirm these results.

A small corroboration of our calculations, however, comes from the Cahill and Pohl [51] amorphous limit for this solid. As it is temperature independent and largely unaffected if $v_s = 4710$ or 5280 m/s, we may deduce that κ_{latt} of MoAlB approaches its fundamental limit at high temperatures. The average v_s should therefore be within 10%–15% of 4700 m/s. Lastly, the calculation and analysis of κ_{latt} suggest a large degree of anharmonicity in the lattice, which coincides with

TABLE II. Summary of physical and thermodynamic property values for MoAlB.

Property (units)	Value
γ (mJ mol^{-1} K^{-2})	1.94 ± 0.01
β (μJ mol^{-1} K^{-2})	18.9 ± 0.5
$N(E_f)$ (eV unit cell)$^{-1}$	3.3
$B_{HT,avg}$ (GPa)	220.3 ± 5.1
θ_D (K) $N_D = 7$	768 ± 1
θ_E (K) $N_E = 2$	241 ± 0.5
$\theta_{D,0}$ (K) when $N_D = 7,9$	621,676
$\Delta H^0_{f,298,MoAlB}$ (kJ/mol)	-132.0 ± 3.2
$H^0_{298,MoAlB}$ (kJ/mol)	9.41
$S^0_{298,MoAlB}$ (J/mol)	53.5
$c^0_{p,\,298\,<\,T\,<\,1800,\,MoAlB}$ (J mol^{-1} K^{-1})[a]	$72.363 + 8.73 \times 10^{-3}\,T - 1.345 \times 10^6\,T^{-2} - 9.8 \times 10^{-7}\,T^2$
$\Delta G^0_{f,100\,<\,T\,<\,1800,MoAlB}$ (kJ/mol)[a]	$130.5 + 9.714 \times 10^{-4}\,T + 8.526 \times 10^{-6}\,T^2$
Γ (unitless Grüneisen parameter)	1.76
$v_{s,300\,K}$ (m/s)[b]	5364
$v_{s,cp}$ (m/s)[c]	4710

[a]Empirical fit ($R^2 = 0.99$) of the results obtained from the explicit calculation mentioned in the text.
[b]Average speed of sound from RUS at 300 K calculated from Eq. (21).
[c]Value that best reproduces experimental κ_{latt} data, see text.

the presence of low-energy optical phonon modes known to be effective for scattering phonons [14].

IV. CONCLUSIONS

In conclusion, differential thermal analysis, x-ray diffraction, and quenching experiments were used to ascertain the thermal melting/decomposition point of MoAlB. Based on these results, we conclude that MoAlB decomposes above $\sim$1708 K in inert and vacuum atmospheres via incongruent melting into MoB (solid) and Al (liquid). The experimental heat capacity of MoAlB was measured up to 1000 K and successfully modeled as the sum of lattice, electronic, and dilation contributions. Moreover, the standard enthalpy of formation at 298 K was determined to be -132.0 ± 3.2 kJ mol^{-1}, and the free energy of formation was calculated over the full temperature range. Additionally, the temperature dependence of thermal conductivity, recalculated using temperature-dependent c_p values, is weak and could be modeled using a variation of the Slack [47] model. The analysis contained

herein gives a consistent story of the presence and implications of low-lying optical phonon modes and their contribution to c_p and thermal conductivity. Table II summarizes the physical property values calculated from the experiments conducted herein.

[1] C. Martini, G. Palombarini, G. Poli, and D. Prandstraller, Wear **256**, 608 (2004).

[2] B. J. Aylett, Br. Polym. J. **18**, 359 (1986).

[3] E. Sani, L. Mercatelli, M. Meucci, A. Balbo, C. Musa, R. Licheri, R. Orrù, and G. Cao, Renew. Energy **91**, 340 (2016).

[4] K. H. J. Buschow, Mater. Sci. Rep. **1**, 1 (1986).

[5] X. W. Yu and S. Licht, J. Power Sources **179**, 407 (2008).

[6] S. Licht, X. Yu, and D. Qu, Chem. Commun. (Cambridge, UK) **2**, 2753 (2007).

[7] Y. Wang, X. Y. Guang, Y. L. Cao, X. P. Ai, and H. X. Yang, J. Appl. Electrochem. **39**, 1039 (2009).

[8] W. G. Fahrenholtz and G. E. Hilmas, Int. Mater. Rev. **57**, 61 (2012).

[9] T. A. Parthasarathy, R. A. Rapp, M. Opeka, and R. J. Kerans, Acta Mater. **55**, 5999 (2007).

[10] S. Kota, E. Zapata-Solvas, A. Ly, J. Lu, O. Elkassabany, A. Huon, W. E. Lee, L. Hultman, S. J. May, and M. W. Barsoum, Sci. Rep. **6**, 26475 (2016).

[11] M. W. Barsoum, Prog. Solid State Chem. **28**, 201 (2000).

[12] D. J. Tallman, B. Anasori, and M. W. Barsoum, Mater. Res. Lett. **1**, 115 (2013).

[13] J. L. Smialek, Corros. Sci. **91**, 281 (2015).

[14] O. Chaix-Pluchery, A. Thore, S. Kota, J. Halim, C. Hu, J. Rosen, T. Ouisse, and M. W. Barsoum, J. Raman Spectrosc. (2017).

[15] W. Jeitschko, Monatsh. Chem. **97**, 1472 (1966).

[16] V. S. Sinel'nikova, V. N. Gurin, A. N. Pilyankevich, L. V. Strashinskaya, and M. M. Korsukova, J. Less-Common Met. **47**, 265 (1976).

[17] Y. Yu and T. Lundström, J. Alloys Compd. **226**, 5 (1995).

[18] S. Okada, Kokushikan Daigaku Kiyo **31**, 7 (1998).

[19] S. Okada, K. Iizumi, K. Kudaka, K. Kudou, M. Miyamoto, Y. Yu, and T. Lundström, J. Solid State Chem. **133**, 36 (1997).

[20] M. Ade and H. Hillebrecht, Inorg. Chem. **54**, 6122 (2015).

[21] J. L. Smialek and A. Garg, Surf. Interface Anal. **47**, 844 (2014).

[22] W. Rieger, H. Nowotny, and F. Benesovsky, Mh. Chem. **96**, 844 (1965).

[23] J. Castaing, R. Caudron, G. Toupance, and P. Costa, Solid State Commun. **7**, 1453 (1969).

[24] B. D. Hanson, M. Mahnig, and L. E. Toth, Z. Naturforsch., A: Astrophys., Phys. Phys. Chem. **26**, 987 (1971).

[25] M. K. Drulis, H. Drulis, A. E. Hackemer, O. Leaffer, J. Spanier, S. Amini, M. W. Barsoum, T. Guilbert, and T. El-Raghy, J. Appl. Phys. **104**, 023526 (2008).

[26] M. K. Drulis, H. Drulis, S. Gupta, M. W. Barsoum, and T. El-Raghy, J. Appl. Phys. **99**, 093502 (2006).

[27] M. Radovic, E. Lara-Curzio, and L. Riester, Mater. Sci. Eng., A **368**, 56 (2004).

[28] P. Gao, A. Bolon, M. Taneja, Z. Xie, N. Orlovskaya, and M. Radovic, Solid State Ionics **300**, 1 (2017).

[29] R. W. Hertzberg, *Deformation and Fracture Mechanics of Engineering Materials*, 5th ed. (Wiley, New York, 1989).

[30] R. Hill, Proc. Phys. Soc., London, Sect. A **65**, 349 (1952).

[31] M. Eumann, G. Sauthoff, and M. Palm, Int. J. Mater. Res. **97**, 1502 (2006).

[32] G. A. Yasinskaya, Sov. Powder Metall. Met. Ceram. **5**, 557 (1966).

[33] G. V Samsonov, A. D. Panasyuk, G. K. Kozina, and L. V. D'yakonova, Sov. Powder Metall. Met. Ceram. **11**, 568 (1972).

[34] H. Okamoto, J. Phase Equilibria Diffus. **31**, 492 (2010).

[35] A. Jain, S. P. Ong, G. Hautier, W. Chen, W. D. Richards, S. Dacek, S. Cholia, D. Gunter, D. Skinner, G. Ceder, and K. A. Persson, APL Mater. **1**, 011002 (2013).

[36] X. Li, H. Cui, and R. Zhang, Sci. Rep. **6**, 39790 (2016).

[37] M. W. Barsoum, *MAX Phases Prop. Mach. Ternary Carbides Nitrides*, 1st ed. (Wiley-VCH, Weinheim, 2013), pp. 107–115.

[38] Y. S. Tyan, E. T. Louis, and Y. A. Chang, J. Phys. Chem. Solids **30**, 785 (1969).

[39] M. K. Drulis, A. Czopnik, H. Drulis, J. E. Spanier, A. Ganguly, and M. W. Barsoum, Mater. Sci. Eng., B **119**, 159 (2005).

[40] M. T. Agne and M. W. Barsoum, J. Alloys Compd. **665**, 218 (2016).

[41] A. S. Bolgar, A. V. Blinder, and M. I. Serbova, Sov. Powder Metall. Met. Ceram. **29**, 977 (1990).

[42] E. G. Lavut, N. V. Chelovskaya, and O. E. Kashireninov, J. Eng. Phys. Thermophys. **65**, 971 (1993).

[43] M. W. Chase, JANAF Thermochemical Tables, Am. Chem. Soc. New York, Am. Inst. Phys. Natl. Bur. Stand. c1986, US Natl. Bur. Stand. (1986), p. 1, http://adsabs.harvard.edu/abs/1986jtt..book.....C.

[44] I. Shilo and H. F. Franzen, J. Electrochem. Soc. **129**, 2613 (1982).

[45] M. W. Barsoum, I. Salama, T. El-Raghy, J. Golczewski, H. J. Seifert, F. Aldinger, W. D. Porter, and H. Wang, Metall and Mat Trans A **33**, 2775 (2002).

[46] M. W. Barsoum, C. J. Rawn, T. El-Raghy, A. T. Procopio, W. D. Porter, H. Wang, and C. R. Hubbard, J. Appl. Phys. **87**, 8407 (2000).

[47] G. A. Slack, *Solid-State Physics*, 1st ed. (Academic, New York, 1979), Vol. 34.

[48] E. S. Toberer, A. Zevalkink, and G. J. Snyder, J. Mater. Chem. **21**, 15843 (2011).

[49] R. Bruls, H. T. Hintzen, and R. Metselaar, J. Appl. Phys. **98**, 126101 (2005).

[50] O. L. Anderson, J. Phys. Chem. Solids **24**, 909 (1963).

[51] D. G. Cahill and R. O. Pohl, Annu. Rev. Phys. Chem. **39**, 93 (1988).